· Article · Advances in Polar Science
doi: 10.12429/j.advps.2023.0015 Septemper 2023 Vol. 34 No. 3: 220-231

# Marginal weakening promoted rift propagation of the Petermann Ice Shelf in northwestern Greenland from 2016 to 2022

LI Daan[1,2], JIANG Liming[2,3*], HUANG Ronggang[2] & LU Xi[2,3]

[1] School of Urban and Reginal Planning, Yancheng Teachers University, Yancheng 224002, China;
[2] State Key Laboratory of Geodesy and Earth's Dynamics, Innovation Academy for Precision Measurement Science and Technology, Chinese Academy of Sciences, Wuhan 430077, China;
[3] College of Earth and Planetary Science, University of Chinese Academy of Sciences, Beijing 100049, China

**Received 5 March 2023; accepted 26 September 2023; published online 30 September 2023**

**Abstract** Ice-shelf rifts are precursors of glacier calving, and thus they serve as indicators of ice shelf instability, especially under oceanic and atmospheric warming conditions. Therefore, understanding the dynamic processes underlying rift propagation and the associated damage mechanisms is essential to evaluate ice-shelf instability and to predict glacier calving. In this study, we investigated the effect of marginal weakening on rift propagation on the ice shelf of the Petermann Glacier, among the largest in Greenland, during 2016–2022. First, we analyzed satellite optical images to monitor rift growth (length and width) by tracking the tip trajectory of three large rifts identified on the Petermann Ice Shelf. Then, we estimated rift depth using ArcticDEM and ICESat-2 data. Our results indicated consistent increases of the rift widths and depths over the study period, with mean values of 133 $m{\cdot}a^{-1}$ and 0.3 $m{\cdot}a^{-1}$, respectively. We also combined remote-sensing observations with an ice-sheet numerical model to calculate the stress and damage fields on the Petermann Ice Shelf and to assess the ice shelf margin stability and strength. We determined that damage and lateral shear in the fracture zone degraded ice shelf integrity by decreasing the contact length with the fjord wall. In conclusion, marginal weakening effectively promoted rift propagation on the Petermann Ice Shelf, increasing the risk of future glacier calving.

**Keywords** rift propagation, marginal weakening, remote sensing, damage mechanism

**Citation:** Li D A, Jiang L M, Huang R G, et al. Marginal weakening promoted rift propagation of the Petermann Ice Shelf in northwestern Greenland from 2016 to 2022. Adv Polar Sci, 2023, 34(3): 220-231, doi: 10.12429/j.advps.2023.0015

## 1 Introduction

Ice-shelf (or glacier) calving in Greenland triggers ice flow acceleration and glacier front retreat (Bondzio et al., 2017). It has become a crucial factor affecting the stability of the Greenland Ice Sheet (Benn et al., 2017). Contribution of glacier calving to ice-sheet mass loss is a major source of uncertainty in sea-level rise projections (Stocker et al., 2013; Pörtner et al., 2019; Pattyn and Morlighem, 2020). Therefore, characterization and accurate forecasting of the calving process is essential for both ice-sheet model development and sea-level projections (Benn and Åström, 2018). In particular, occurrence of calving along rifts reduces buttressing on the grounded glacier and enhances discharge from the ice sheet interior into the ocean (Rignot and Kanagaratnam, 2006; Greene et al., 2022). Thus, rift propagation is an important dynamic process that must be considered in ice-shelf calving studies (Borstad et al., 2017; Larour,et al., 2021).

Although previous research combining observations

* Corresponding author, E-mail: jlm@whigg.ac.cn

and modeling suggested that tidewater glaciers are sensitive to atmospheric and oceanic forcing (Cowton et al., 2017), the physical mechanism process governing rift propagation and its response to glacier damage and marginal weakening is not fully understood (Zarrinderakht et al., 2022). Current calving models, such as the height-above-buoyancy criterion (Vieli et al., 2001), eigen-calving (Levermann et al., 2012), or von Mises stress (Morlighem et al., 2016), can replicate glacier advance and retreat, but they are not adapted to diagnose the stability of fractures and ice shelves.

Numerous observation and modeling results have established that marginal weakening damages ice-shelf integrity and promotes rift propagation (Vieli et al., 2007; Lipovsky, 2020; Humbert et al., 2023). In turn, rift propagation demonstrably plays a crucial role in complicated ice-shelf calving and collapsing processes (Banwell et al, 2013; Leeson et al., 2020). This was illustrated, for example, for the Larsen B Ice Shelf: ice rheology inversions determined considerable marginal weakening prior to its collapse (Khazendar et al., 2007). Glasser and Scambos (2008) further speculated that this marginal weakening immediately preceded rift propagation, triggering the subsequent calving of Larsen B that led to its complete collapse (Glasser and Scambos, 2008). Numerous observations and detailed model analysis confirmed that marginal weakening precedes ice rift propagation, notably in narrow configurations when the ice shelf margin is nearly parallel to the ice flow along a fjord wall (Lipovsky, 2020). Compared with the open geometry of extensive Antarctic ice shelves such as Larsen C Ice Shelf and Amery Ice Shelf, frictional drag and shear within narrow fjords in Greenland cause more serious damage and marginal weakening, intensifying crevasse development and rift propagation (Johnson et al., 2011; Åkesson et al., 2018). Specifically, evidence of the relationship between ice front retreat, rift growth, and marginal thinning was established for the Jakobshavn Glacier in Greenland (Joughin et al., 2008; MacGregor et al., 2012). Although surface rifts penetrate tens of meters into the ice, generating tensile stress on ice shelves and glaciers, their presence has little effect on glacier calving. Conversely, crevasse or rift advection accelerates glacier calving (Berg and Bassis, 2022).

This article is organized as follows: in this section, we have explained the importance of ice shelf instability and glacier calving and summarized previous research on the relationship between glacier marginal weakening, damage mechanisms, and rift propagation. Next, we describe the study site, the analysis data and tools (remote sensing images and ice flow model), and the methodology in Section 2. In Section 3, we present the results on rift propagation (advection distance and width, depth, and area of the rifts), ice flow speed, and comprehensive stress and damage distributions. We discuss the relationship between marginal weakening and rift propagation in Section 4. Finally, we conclude (Section 5) that marginal damage of the Petermann Ice Shelf in northwestern Greenland promoted rift propagation and will induce future calving.

# 2 Location, data and method

## 2.1 Study site

The Petermann Glacier, located in northern Greenland (Figure 1), is approximately 70 km in length and includes a floating ice tongue with a width of 15 km and a thickness ranging from 600 m at its grounding line to approximately 30–80 m at the ice front (Rignot and Steffen, 2008). It is the second-largest floating ice shelf in Greenland and discharges approximately 4% of the Greenland Ice Sheet into the ocean (Münchow et al., 2014). Approximately 80% of the mass flux across the Petermann Ice Shelf is produced by basal melting (Rignot and Steffen, 2008); the remainder (approximately 20%) is attributed to sporadic calving events and to surface meltwater runoff and drainage in summer (Washam et al., 2019). Currently, the majority of mass loss, including ice front collapse and grounding line retreat (Ciracì et al., 2023), is caused by increases in the oceanic heat flux and in the calving rate on the Petermann Ice Shelf (Holland et al., 2008; Straneo and Heimbach, 2013).

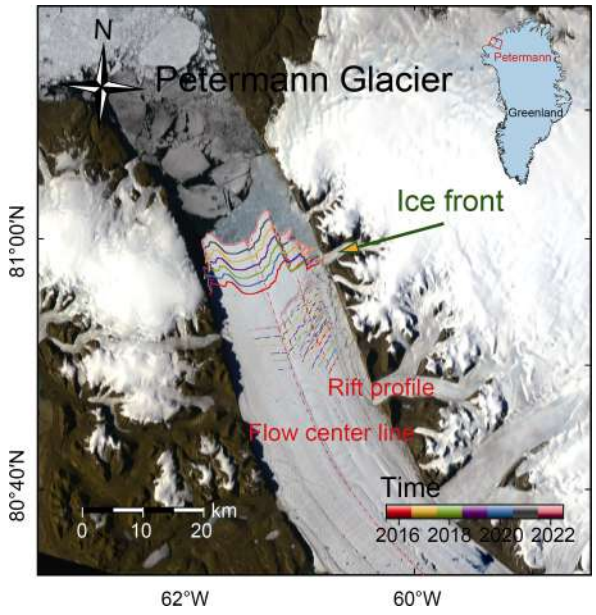


**Figure 1** Petermann Glacier and ice shelf, with its location in northwestern Greenland (inset, red box). The center of the ice flow (longitudinal dot-dashed red line, flow center line) and consecutive positions of the ice front (solid lines) and rifts (dot-dashed lines), color-coded from 2016 to 2022, are superimposed on a Landsat-8 satellite image acquired in 2022.

The Petermann Ice Shelf lost approximately 40% of its tongue during two massive calving events in 2010 and 2012 (Nick et al., 2012). A smaller calving event occurred on 26 July 2017 along a preexisting rift (Li et al., 2021). Furthermore, new rifts have recently developed between the center of the ice shelf and its eastern margin, indicating a

probable forthcoming calving event (Rückamp et al., 2019; Åkesson et al., 2022; Millan et al., 2022). The incessant collapse events of the Petermann Ice Shelf intensified the ice front to retreat, by severing the connection with the eastern fjord wall and decreasing the drag and buttressing on the upstream glacier (Hill et al., 2018).

### 2.2 Satellite optical images and laser altimetry data

In this study, we first delineated rift positions and derived ice velocity on the Petermann Glacier during 2016–2022. For this purpose, we used optical images from the identical Sentinel-2A and Sentinel-2B satellites launched in June 2015 and March 2017, respectively, by the European Space Agency within the framework of its Copernicus Programme (Drusch et al., 2012). We selected Sentinel-2A/B images with a cloud cover of 10% or less acquired in the near-infrared band during the summer months (June–August) during 2016–2022, retrieved from the European Space Agency Copernicus Open Access Hub (https://scihub.copernicus.eu/dhus/#/home). Then, from visual interpretation, we identified the distribution and geometry of rifts on the Petermann Ice Shelf and calculated their width, length, and area.

We subsequently applied a feature tracking algorithm (Leprince et al., 2008) to the Sentinel-2A/B images to derive annual mean ice flow speed as follows: (1) the ice velocity field was first determined with the COSI-Corr software (Leprince et al., 2008; Mouginot et al., 2012); (2) the Rosenau filter algorithm was then applied, consisting of image segmentation into smooth growth regions, median calculation, and application of directional constraints to remove speed outliers from the initial speed field (Lüttig et al., 2017); (3) finally, an inverse-distance weighing algorithm (Bartier and Keller, 1996) was used to interpolate the velocity field.

In a second step, we calculated rift depths in 2021 by comparing ice shelf elevation from satellite remote-sensing data and bottom elevation from a digital elevation model (DEM). Ice shelf elevation was measured by the second ICESat-2 (the NASA Ice, Cloud, and land Elevation Satellite-2), and launched in September 2018. The single instrument carried by ICESat-2, a laser altimeter with high spatial and temporal resolution, provides detailed observation of the dense ice shelf rift topography in Greenland (Markus et al., 2017). For this analysis, we extracted ice shelf elevation from ICESat-2 Level 3A data version ATL06, released in 2019 (Brunt et al., 2019). Bottom elevation was derived from ArcticDEM data, a timestamped DEM collection with high spatial resolution (2 m and 10 m) covering the period 2009–2017, thus with a high potential for monitoring ice surface height, structural morphology evolution (Porter et al., 2022). ArcticDEM data are stored in the Google Earth Engine cloud computing platform, together with JavaScript and Python coding tools that provide opportunities for rapid analysis. Here, we extracted bottom elevation from the ArcticDEM v3 mosaic data. Then, we calculated rift depths by subtracting the ArcticDEM bottom elevation from the ICESat-2 ice shelf surface elevation (Herzfeld et al., 2021; Marsh et al., 2021).

### 2.3 Numeral modeling of the ice flow

We applied the Ice-sheet and Sea-level System Model to calculate the spatiotemporal distribution of stress and damage (Borstad et al., 2016; Larour et al., 2021) on the Petermann Ice Shelf. Ice flow was modeled with the two-dimensional Shelfy-Stream Approximation (MacAyeal, 1989). We assumed constant rheology, depending only on the ice steady-state temperature, and combined it with the observed ice velocity to calculate the floating-ice stress field using Glen's flow law (Cuffey and Paterson, 2010). The analytical solution of the forward model yielded estimates for the effective deviatoric stress and for scalar damage, allowing to quantify and diagnose the instability of the ice shelf and rifts. We derived simplified expressions for the effective stress and scalar damage (Cuffey and Paterson, 2010; De Rydt et al., 2018) from the ice constitutive equations:

$$\dot{\delta}_{\mathrm{e}} = \sqrt{\frac{\dot{\delta}_{xx}^2 + 2\dot{\delta}_{xy}^2 + \dot{\delta}_{yy}^2}{2}}, \tag{1}$$

$$\delta' = 2u\dot{\varepsilon}, \tag{2}$$

$$u = \frac{B}{2\dot{\varepsilon}_{\mathrm{e}}^{(n-1)/n}}, \tag{3}$$

$$D = 1 - \left[\frac{\theta}{\dot{\varepsilon}_{xx}}\right]^{\frac{1}{n}} \left[\frac{1}{\frac{2\rho g H}{B}}\right] \tag{4}$$

In Equation (1), $\dot{\delta}_{\mathrm{e}}$, $\dot{\delta}_{xx}$, $\dot{\delta}_{xy}$, and $\dot{\delta}_{yy}$ represent the effective, transverse, shear, and longitudinal stress, respectively. Equation (2) expresses the deviatoric stress tensor $\delta'$, depending on $\dot{\delta}_{xx}$, $\dot{\delta}_{xy}$, and $\dot{\delta}_{yy}$, as a function of $u$, the effective ice viscosity, defined from the generalized version of Glen's flow law (Glen, 1955) by considering ice as a non-Newtonian fluid, and of $\dot{\varepsilon}$, the strain rate tensor, derived from the ice velocity field. The effective viscosity $u$ is defined in Equation (3), where $n$ is Glen's flow law exponent, generally assumed equal to 3; $B$ is the ice rigidity, calculated from the ice temperature (set to −5 °C in this study) using Cuffey's flow law (Rückamp et al., 2019); and $\dot{\varepsilon}_{\mathrm{e}}$ is the effective strain rate. Finally, scalar damage $D$ is defined in Equation (4), with $\dot{\varepsilon}_{xx}$ the transverse strain rate; $\theta$ the contribution term for the shear and lateral strain rates; $\rho$ the ice density; $g$ the gravitational acceleration; and $H$ the ice thickness.

Initial model parameter values (ice thickness, ice topography, and boundary conditions) were extracted from the BedMachine v3 Greenland geometry dataset (Morlighem et al., 2017). Observed velocity was prescribed

at the ice boundary (Hill et al., 2018; Rückamp et al., 2019). Model calculations were performed on an adaptive finite-element grid covering the full Petermann Glacier basin and comprising 110676 elements. Model mesh grid resolution was 2000 m in slow-moving regions, 50 m in fast-flowing regions, and refined to 20 m in the rift region (Figure S1).

# 3 Results

## 3.1 Rift advection and propagation

First, taking advantage of the observation geometry differences between Sentinel-2A and Sentinel-2B, we visually examined the fracture zone on the Petermann Ice Shelf and manually delineated the observed rift positions on pairs of images (one image per Sentinel-2 satellite) acquired every year during 2016–2022 (Figure 2). From the Sentinel-2A/B images, the ICESat-2 altimetry data, and the ArcticDEM dataset, we evaluated rift length, width, area, and estimated their depth from ice shelf surface to rift bottom. We identified three distinct rifts: two large ones extending from the center to the right side of the ice flow (hereafter upstream and downstream rifts), and one on the left of the ice flow centerline (hereafter middle rift). Their estimated annual mean positions during the 2016–2022 study period are illustrated in Figure 2, superimposed on ArcticDEM data for 2017. Temporal evolution of the rift geometric properties (advection distance, width, and area) is plotted in Figure 3. The length and width of the three rifts increased nearly continuously over the study period. In 2016, two rifts were visible, both on the right side of the glacier, a moderate-length upstream rift and a longer one further downstream. The middle rift appeared in 2017, developed from the center to the left side of the ice flow, and connected with the lengthening downstream rift in 2020 (Figure 2). Concurrently with the ice flow, rifts were advected downstream during the study period.

From Sentinel-2 images, we estimated that the length of the rift increased from its initial value of 3 km to approximately 5 km over the study period (Figure 2). The width of the upstream rift, calculated from the differences in position between two images of a pair, increased from 100 m to 900 m between 2016 and 2022 (Figure 3). Concurrently, the total fracture zone area increased from 1 $km^2$ to 5 $km^2$ as the upstream and downstream rifts widened and were advected toward the ice front (Figure 3). Additionally, we calculated propagation rates as the interannual distance difference between two consecutive upstream and downstream points. Propagation rate was largest (approximately 110 $m \cdot a^{-1}$) when the rift activated, then rapid expansion occurred separately for each rift after 2019. The rifts continued to expand, by approximately 100 $m \cdot a^{-1}$, during the intermediate propagation stage.

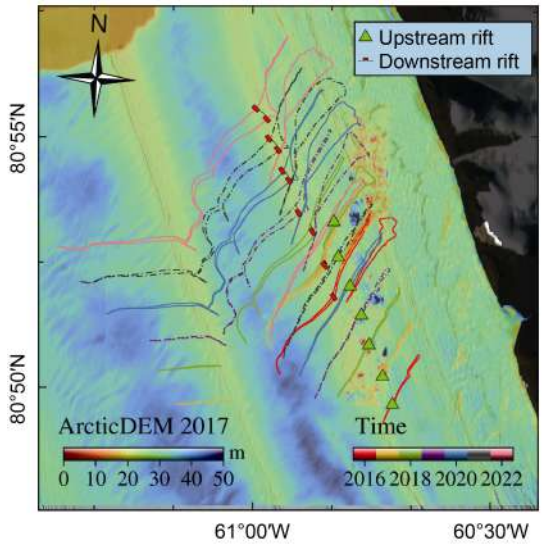


**Figure 2** Position and temporal evolution of the Petermann Ice Shelf rifts, color-coded by year (bottom-right color bar) during 2016–2022 and overlaid on a color map for 2017 (bottom-left color bar) extracted from a digital elevation model (ArcticDEM). The background image (gray) was acquired by Sentinel-2, also in 2017. Three major rifts were identified, one appearing near the center of the ice shelf (middle rift), two developing from the east margin of the ice shelf toward the center, the upstream (green triangles) and downstream (red rectangles) rifts.

Between 2015 and 2017, rift bottom elevation extracted from the ArcticDEM dataset decreased from 18.84 m to 16.90 m (Figure 4). From ICESat-2 altimetry measurements, we extracted topographic information across the rift (calculated depth also shown in Figure 4) to analyze the temporal evolution of elevation along the rift cross-section (surface elevation on the southern and northern edges and bottom elevation). Two consecutive ICESat-2 measurements in July 2021 yielded similar elevation values for ice mélange filling the rift (14.65 m and 14.55 m), indicating that the downstream rift had gradually deepened (by 0.35 $m \cdot a^{-1}$) from 2015 to 2021.

## 3.2 Glacier velocity field and stress distribution in the fracture zone

The mean ice speed field on the Petermann Glacier was calculated (Section 2.2) during 2016–2022 during the melt season and is shown in Figure 5. As expected, calculated downstream ice flow speed were clearly higher than upstream ice shelf speed, which were reduced by the presence of rifts. Speed along the flow centerline (Figure 1) exhibited a globally increasing trend, with maximum downstream speed of approximately 1800 $m \cdot a^{-1}$ reached during 2019–2020. This strong increase in the center speed likely indicates a past disintegration event.

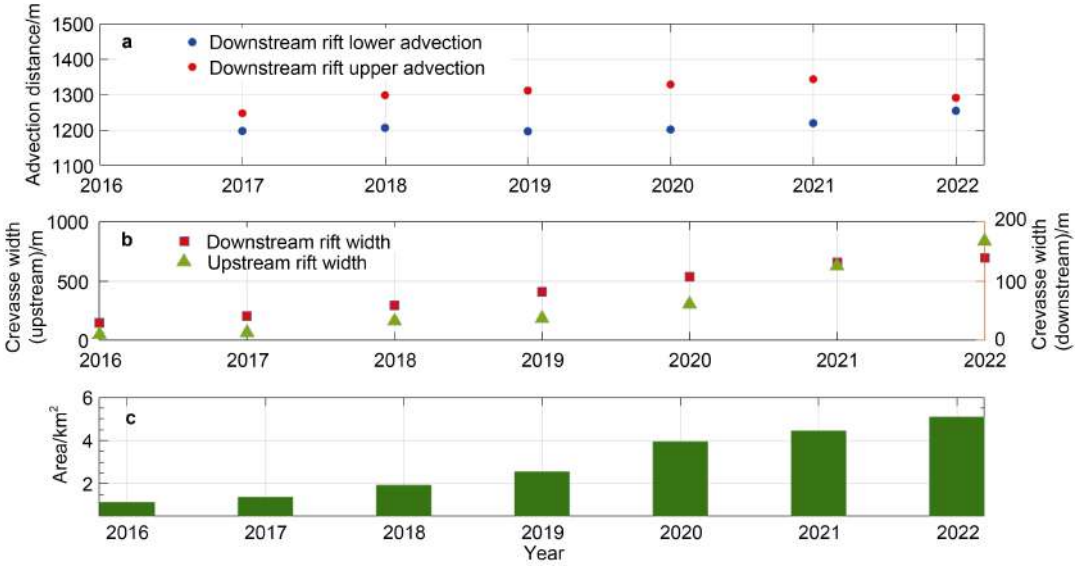


**Figure 3** Temporal evolution in the fracture zone of the Petermann Ice Shelf during 2016–2022 of the advection distance on the lower (blue) and upper (red) sides of the downstream rift (**a**), the downstream (red squares) and upstream (green triangles) rift widths (**b**), and the total rift area (**c**).

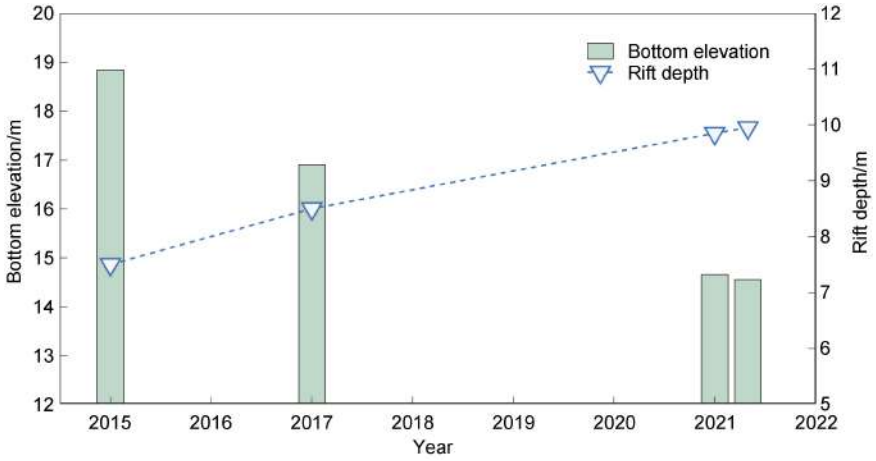


**Figure 4** Bottom elevation and calculated depth of the downstream rift on the Petermann Ice Shelf from ArcticDEM (2015, 2017) and ICESat-2 (2021) data.

Subsequently, to analyze dynamic mechanisms influencing rift distribution, we calculated the transverse, longitudinal and shear stress fields using ice rheology and strain rates derived from the velocity field. In this study, stress calculation errors were caused mainly by uncertainties on the velocity field and on glacier rigidity (Equations (2) and (3), Section 2.3). The observed velocity results derived from optical images with the feature tracking algorithm were reliable and glacier rigidity was spatially consistent, ensuring a stress accuracy evaluation by error propagation sufficiently reliable for qualitative discussions. Our calculations indicated an unusual tensile stress burden in the fracture zone. As the rifts were advected and propagated downstream, stress gradually increased and the high-stress region spread, notably along the rifts and ice flow margins.

Figure 6 illustrates the annual mean transverse stress distribution, stretching across the east side of the ice flow and onto the ice shelf where it formed a transverse extension zone with large rifts, especially in 2019, explaining the preferential east–west orientation of rift propagation.

Figure 7 indicates that high annual-mean longitudinal stress values were concentrated in an ice divergence zone where rifts expanded. In particular, considerable longitudinal stress occurred along the transverse rift (west–east orientation) in 2021 (Figure 7e). Furthermore, marked velocity discontinuities were observed in the rift region (Figure 5), in good correspondence with the high stress regions of Figures 6–7. Longitudinal tensile stress should play a key role in future calving events on the Petermann Ice Shelf.

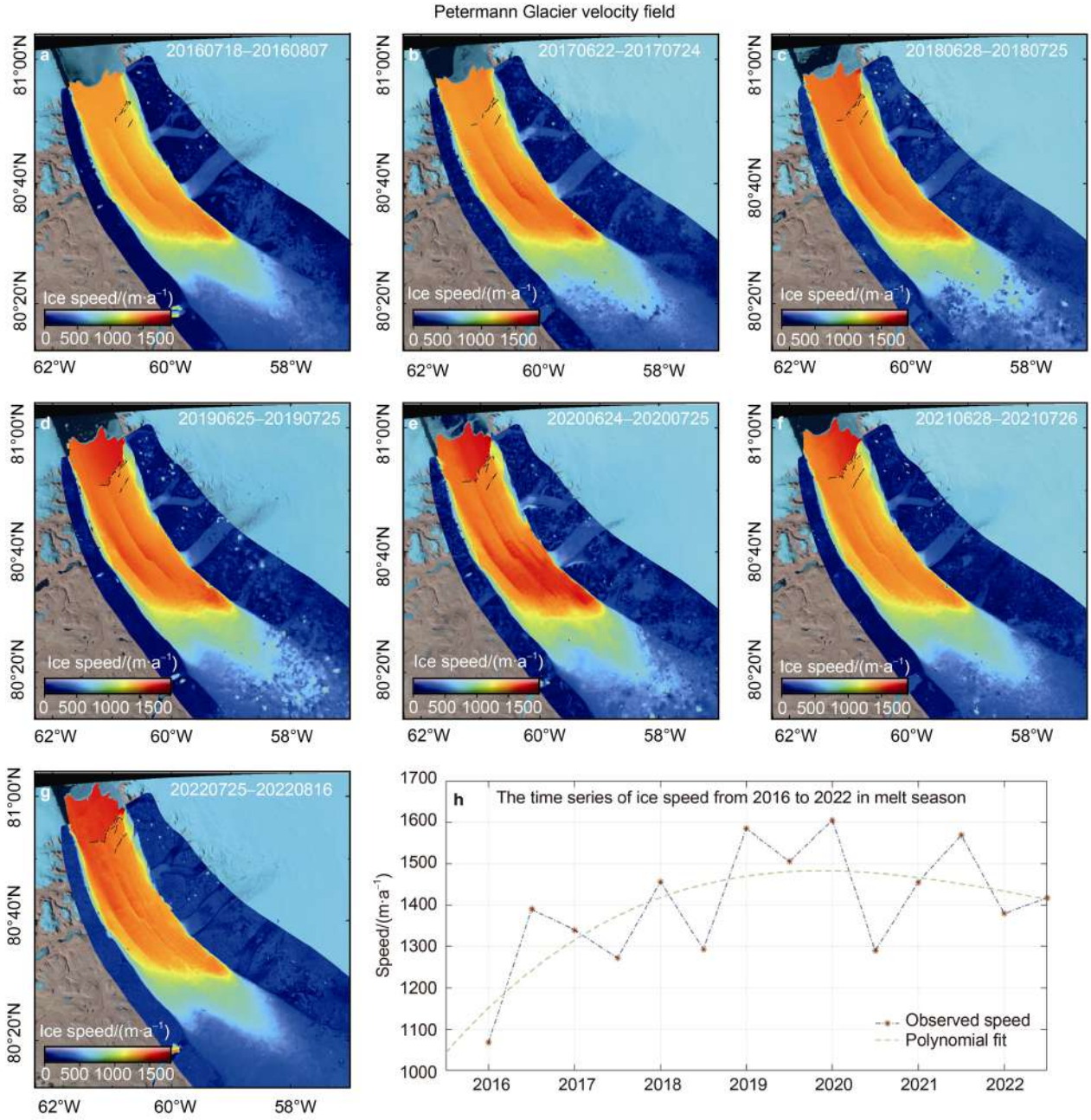


**Figure 5** Spatial distribution and temporal evolution during 2016–2022 of ice velocities calculated from Sentinel-2A/B images during the melt season on the Petermann Ice Shelf. Mean velocity field for each year (**a**–**g**). The color bar (bottom left) shows the velocity range. **h**, time series of the mean speeds along the ice flow centerline (Figure 1). The red dots represent mean values calculated for each year. The green dashed line is a polynomial fit to the mean values.

Figure 8 indicates high shear stress regions where the ice shelf connected with the fjord wall (ice shelf eastern margin) during 2017–2022. The downstream rift rotated anticlockwise under the influence of unbalanced forces from different directions, resulting in the eastern margin region with degraded stability (Figure 8). Owing to its intrinsic characteristics, shear stress acted as a preconditioning factor that weakened the integrity and rigidity of the ice shelf margin. Splashing rifts created a strong shearing zone adjacent to the eastern fjord wall (Figure 8). Local high-shear stress regions promoted rift opening and propagation near the shear margin, causing damage in the convergence zone. Rift propagation in the horizontal plane is normally parallel to the principal axes of least tensile stress and perpendicular to the principal axes of highest tensile strain rate. Shear stress, mainly affecting glacier margins, also initiated rift propagation toward the center of the ice shelf. Thus, the downstream part of the

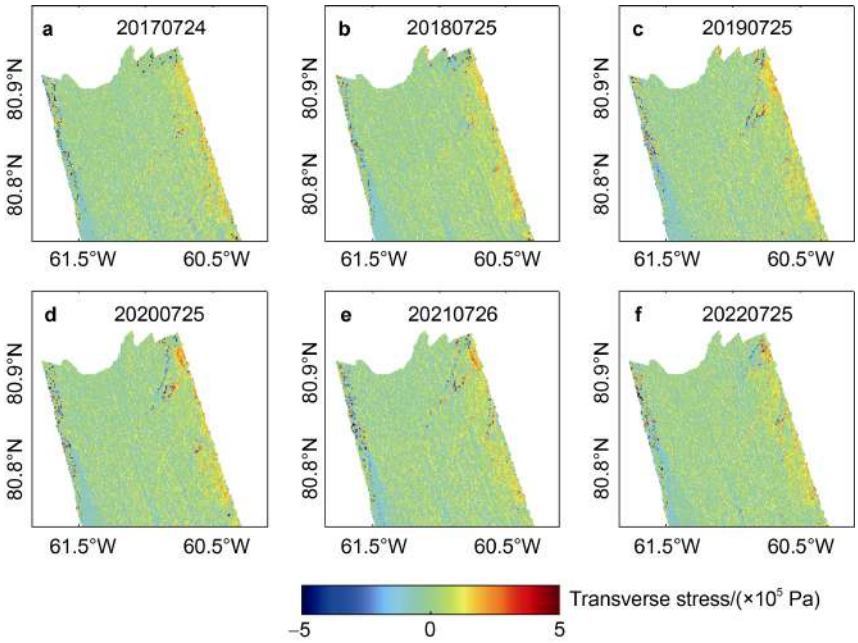


**Figure 6** Spatial distribution during 2017–2022 of the mean transverse stress field calculated every year in July from 2017 (**a**) to 2022 (**f**) on the Petermann Ice Shelf.

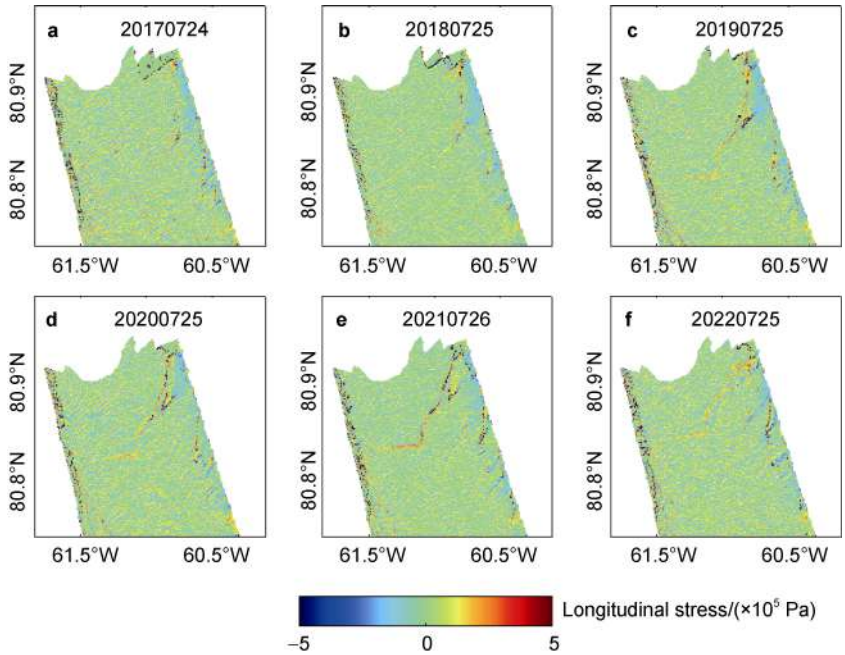


**Figure 7** Same representation as in Figure 6, but for the mean longitudinal stress field.

glacier contrarotated along the downstream rift located within the ice flow, generating strong shear stress, negative at the eastern ice shelf margin and positive at the western margin (Karunamoorthy, 2019).

Figure 9 illustrates the clear, continuously increasing trend on the effective stress at the ice margin between 2017 and 2022. Structural ice-shelf weakness was mainly distributed in the fracture zone where the effective stress field exhibited consistently high values, within 300–600 kPa in the shear zone. The rheology of an ice margin might become unstable under an increasing effective stress burden, while the effective stress itself, in turn, is sensitive to the plastic rheology of a rift. Moreover, the direct effect of effective stress field variations was to instantaneously destabilize the ice shelf margin and rift rheology. In summary, effective stress acted as a preconditioning factor, causing fracture instability in damaged shear zones of the Petermann Ice Shelf.

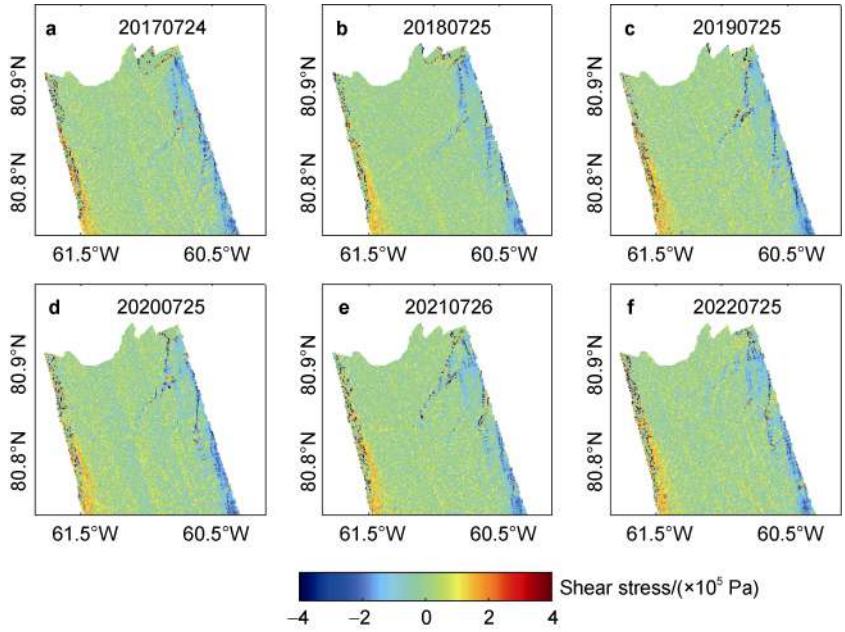


**Figure 8** Same representation as in Figure 6, but for the mean shear stress field.

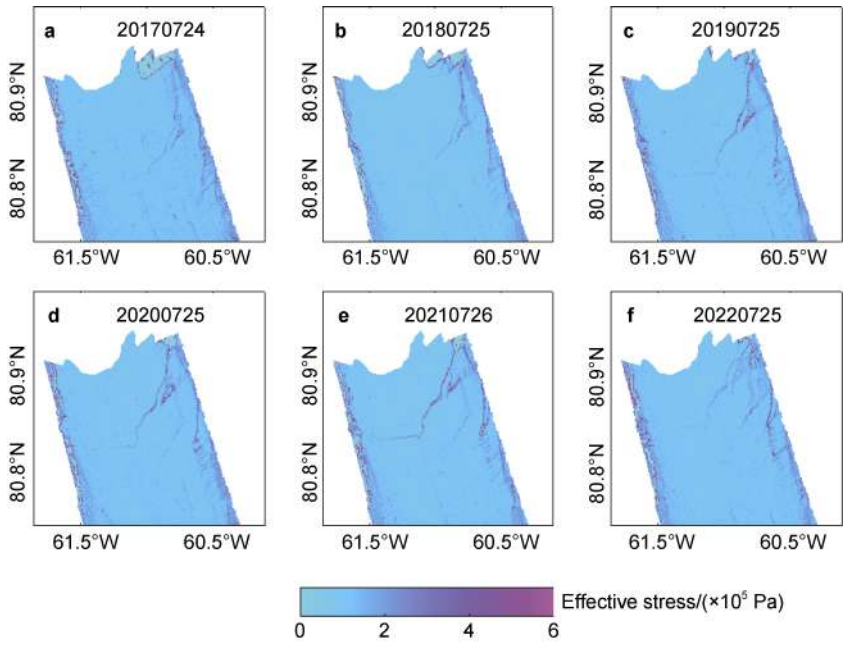


**Figure 9** Same representation as in Figure 6, but for the mean effective stress field.

### 3.3 Scalar damage variations in the rift and marginal regions

Using Equations (1) and (4), we applied the analytical scalar damage solutions during each melt season during 2017–2022 to derive scalar damage fields (Figure 10), evaluate fracture stability, assess the ice-shelf marginal strength, and quantify the influence of ice-shelf stress on fracture stability. Damage and weakening phenomena were located in the wrinkle region, the frontal and marginal shear zones of the Petermann Ice Shelf. Initially, in 2017, damage was restricted to Petermann Ice Shelf regions exhibiting only minor damage indications of rifts (Figure 10a) except in the frontal calving region (Li et al., 2021). Then, the damage zone gradually extended toward the middle of the ice shelf (Figure 10b). Concurrently with rift propagation, scalar damage gradually increased, with largest values (0.5 or more) reached in the damage zone surrounding wider rifts, especially from 2019 to 2022 (Figures 10c–10f). Conversely, shearing and wrinkling along the fjord wall generated friction with the upstream glacier flow, weakening the margin structure and the glacier rheology. In

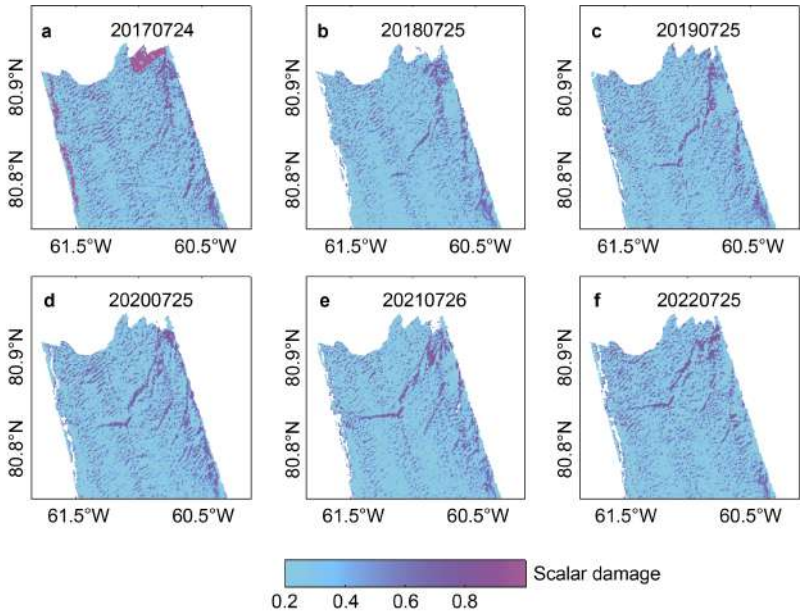


**Figure 10** Same representation as in Figure 6, but for the mean scalar damage distribution.

this shear and wrinkle zone, scalar damage remained consistently high during 2017–2022, with highest values exceeding 0.8 at the tip and in the middle of the rift, through the gradually increasing effective stress burden. The eastern glacier margin started losing viscosity and buttressing failed. Although some slant wrinkles and seams had already developed in 2017, their formation accelerated after the downstream and middle rifts widened and lengthened (and subsequently connected) in 2019.

Figure 10 also indicates that, since 2017, the ice shelf margin weakened and its integrity degraded, consistently with increasing scalar damage that finally exceeded the buttressing effect at the ice front and shear zone. In 2018, a severe damage region clearly appeared in the vicinity of downstream and middle rifts, with scalar values exceeding the 0.5 threshold, ultimately reaching a "completely damaged" state (value of 1). The existence of a severely damaged area implied that the rifts could not sustain the interior stress burden, triggering subsequent rift propagation. When rifts connect with a damaged shear zone, the ice front, structurally weakened, is no longer stable and causes large calving events. In this study, the high effective stress and scalar damage in the frontal region demonstrated the underlying vulnerable condition of the Petermann Glacier ice flow, representative of an instability level generally observed before strong calving events.

# 4 Discussion

Stress burden in the fracture zone causes glacier instability and creates lateral drag from the fjord wall, triggering rift growth at the ice shelf margin. Unbalanced stress, applying to the marginal shear zone, weakens glacier rigidity and causes structural damage to the floating region of an ice shelf (Borstad et al., 2016). Additionally, degraded glacier rheology reduces buttressing of floating tributary glaciers along the side wall of the fjord. Creep velocity of the Petermann Ice Shelf, generated by drive stress from the upstream glacier, induced rift advection, thereby decreasing the contact length between the ice shelf and the fjord wall (Berg and Bassis, 2022). Ice shelf rifts subsequently became unstable following marginal weakening or retreated upstream, deep into the embayment. This explains the increased ice flow velocity calculated in our analysis and the separation between the floating ice tongue and fjord walls on both sides, illustrated in Figure 5.

Weakened ice rheology caused a failure of the bonding force created by glacier contact and viscosity, contributing to glacier stretching and rift development induced by the imbalance between upstream drive stress and lateral drag decrease. In particular, a retreat of the Petermann Glacier front was observed on its eastern side, disrupting the stress balance and causing the 2017 calving event (Li et al., 2021). Moreover, three distinct blocks developed in the Petermann Glacier directly because of the negative effect of ocean warming on rift and ice shelf stability (Millan et al., 2022).

Furthermore, the Petermann Ice Shelf is vulnerable to meltwater-driven fracture rifts reaching the waterline, presumably causing hydrofracturing and full rift penetration (Alley et al., 2018; Robel and Banwell, 2019). Rifts penetrate deep into the glacier where the largest effective stress component becomes negligible. Under oceanic and atmospheric warming conditions, basal melting thus induced ice shelf instability (Åkesson et al., 2021, 2022). In this study, reduced marginal strength subsequently enhanced rift propagation when shear stress was applied to the ice shelf margin, especially rift advection out of the embayment (Lipovsky, 2020; Larour et al., 2021). Therefore,

stress imbalance and lateral drag from the fjord walls induced substantial rift growth. In summary, our results indicate that marginal weakening is a precursor of rift propagation and, eventually, of a future collapse of the Petermann Glacier.

# 5 Conclusion

In this study, we analyzed the effect of marginal weakening on rift propagation on the Petermann Ice Shelf, in northwestern Greenland, from 2016 to 2022. By analyzing multiple satellite remote-sensing datasets, we calculated ice flow speeds and rift properties (width, area, and depth) and characterized the rift propagation and advection processes. Additionally, by determining the stress and damage distributions at the surface of the floating ice tongue with a numerical ice-flow model, we established their effect on marginal weakening of the Petermann Glacier. We concluded that stress imbalance, shear, and lateral drag from the fjord walls induced rift growth at the ice shelf margin, weakening the margin and destabilizing the frontal shear zone.

By combining remote-sensing observations with a numerical ice-flow model, we proposed an innovative framework to characterize and assess the marginal strength, generalizing to other ice shelf with completely different geometries. Our results are important to better understand rift propagation mechanisms and to predict future calving events on the Petermann Glacier.

**Acknowledgments** This work was funded by the National Key R&D Program of China (Grant nos. 2018YFC1406102, 2017YFA0603103) and the grand from State Key Laboratory of Geodesy and Earth's Dynamics (Grant no. SKLGED2022-2-2). We thank Guest Editor, Dr. Zhuoqi Chen and three anonymous reviewers for reviewing this manuscript.

## References

Åkesson H, Nisancioglu K H, Nick F M. 2018. Impact of fjord geometry on grounding line stability. Front Earth Sci, 6: 71.

Åkesson H, Morlighem M, O'Regan M, et al. 2021. Future projections of petermann glacier under ocean warming depend strongly on friction law. J Geophys Res Earth Surf, 126(6): e2020JF005921, doi:10.1029/2020jf005921.

Åkesson H, Morlighem M, Nilsson J, et al. 2022. Petermann ice shelf may not recover after a future breakup. Nat Commun, 13: 2519, doi:10.1038/s41467-022-29529-5.

Alley K E, Scambos T A, Miller J Z, et al. 2018. Quantifying vulnerability of Antarctic ice shelves to hydrofracture using microwave scattering properties. Remote Sens Environ, 210: 297-306, doi:10.1016/j.rse.2018.03.025.

Banwell A F, MacAyeal D R, Sergienko O V. 2013. Breakup of the Larsen B Ice Shelf triggered by chain reaction drainage of supraglacial lakes. Geophys Res Lett, 40(22): 5872-5876, doi:10.1002/2013gl057694.

Bartier P M, Keller C P. 1996. Multivariate interpolation to incorporate thematic surface data using inverse distance weighting (IDW). Comput Geosci, 22(7): 795-799, doi:10.1016/0098-3004(96)00021-0.

Benn D I, Cowton T, Todd J, et al. 2017. Glacier calving in Greenland. Curr Clim Change Rep, 3(4): 282-290, doi:10.1007/s40641-017-0070-1.

Benn D I, Åström J A. 2018. Calving glaciers and ice shelves. Adv Phys X, 3(1): 1513819, doi:10.1080/23746149.2018.1513819.

Berg B, Bassis J. 2022. Crevasse advection increases glacier calving. J Glaciol, 1-10, doi:10.1017/jog.2022.10.

Bondzio J H, Morlighem M, Seroussi H, et al. 2017. The mechanisms behind Jakobshavn Isbræ's acceleration and mass loss: a 3-D thermomechanical model study. Geophys Res Lett, 44(12): 6252-6260.

Borstad C, Khazendar A, Scheuchl B, et al. 2016. A constitutive framework for predicting weakening and reduced buttressing of ice shelves based on observations of the progressive deterioration of the remnant Larsen B Ice Shelf. Geophys Res Lett, 43(5): 2027-2035, doi:10.1002/2015gl067365.

Borstad C, McGrath D, Pope A. 2017. Fracture propagation and stability of ice shelves governed by ice shelf heterogeneity. Geophys Res Lett, 44(9): 4186-4194, doi:10.1002/2017gl072648.

Brunt K M, Neumann T A, Smith B E. 2019. Assessment of ICESat-2 ice sheet surface heights, based on comparisons over the interior of the Antarctic ice sheet. Geophys Res Lett, 46(22): 13072-13078, doi:10.1029/2019gl084886.

Ciracì E, Rignot E, Scheuchl B, et al. 2023. Melt rates in the kilometer-size grounding zone of Petermann Glacier, Greenland, before and during a retreat. Proc Natl Acad Sci USA, 120(20): e2220924120, doi:10.1073/pnas.2220924120.

Cowton T, Sole A, Nienow P, et al. 2017. Controls on the transport of oceanic heat to Kangerdlugssuaq Glacier, East Greenland. J Glaciol, 62(236): 1167-1180, doi: 10.1017/jog.2016.117.

Cuffey K, Paterson W S B. 2010. The physics of glaciers, 4th edn. Amsterdam: Academic Press.

De Rydt J, Gudmundsson G H, Nagler T, et al. 2018. Recent rift formation and impact on the structural integrity of the Brunt Ice Shelf, East Antarctica. Cryosphere, 12(2): 505-520, doi:10.5194/tc-12-505-2018.

Drusch M, Bello U D, Carlier S, et al. 2012. Sentinel-2: ESA's optical high-resolution mission for GMES operational services. Remote Sens Environ, 120: 25-36, doi:10.1016/J.RSE.2011.11.026.

Glasser N F, Scambos T A. 2008. A structural glaciological analysis of the 2002 Larsen B ice-shelf collapse. J Glaciol, 54(184): 3-16, doi:10.3189/002214308784409017.

Glen J W. 1955. The creep of polycrystalline ice. Proc Roy Soc London Ser A Math Phys Sci, 228: 519-538.

Greene C A, Gardner A S, Schlegel N J, et al. 2022. Antarctic calving loss rivals ice-shelf thinning. Nature, 609(7929): 948-953, doi:10.1038/s41586-022-05037-w.

Herzfeld U C, Trantow T, Lawson M, et al. 2021. Surface heights and crevasse morphologies of surging and fast-moving glaciers from ICESat-2 laser altimeter data–Application of the density-dimension algorithm (DDA-ice) and evaluation using airborne altimeter and Planet SkySat data. Sci Remote Sens, 3: 100013, doi:10.1016/j.srs.2020.100013.

Hill Emily A, Hilmar G G, Rachel C J, et al. 2018. Velocity response of Petermann Glacier, northwest Greenland, to past and future calving events. Cryosphere, 12(12): 3907-3921.

Holland P R, Jenkins A, Holland D M. 2008. The response of ice shelf basal melting to variations in ocean temperature. J Clim, 21(11):

2558-2572, doi:10.1175/2007jcli1909.1.

Humbert A, Helm V, Neckel N, et al. 2023. Precursor of disintegration of Greenland's largest floating ice tongue. Cryosphere, 17: 2851-2870, doi:10.5194/tc-17-2851-2023.

Johnson H L, Münchow A, Falkner K K, et al. 2011. Ocean circulation and properties in Petermann Fjord, Greenland. J Geophys Res, 116(C1): C01003, doi:10.1029/2010jc006519.

Joughin I, Howat I, Fahnestock M, et al. 2008. Continued evolution of Jakobshavn Isbrae following its rapid speedup. J Geophys Res, 113: 1-14, doi:10.1029/2008JF001023.

Karunamoorthy S. 2019. A rule based method to construct the Mohr's circle for plane stress. Glob J Eng Sci, 4(2): 1-9, doi:10.33552/gjes.2019.04.000581.

Khazendar A, Rignot E, Larour E. 2007. Larsen B Ice Shelf rheology preceding its disintegration inferred by a control method. Geophys Res Lett, 34(19): L19503-1, doi: doi:10.1029/2007GL030980.

Larour E, Rignot E, Poinelli M, et al. 2021. Physical processes controlling the rifting of Larsen C Ice Shelf, Antarctica, prior to the calving of iceberg A68. Proc Natl Acad Sci USA, 118(40): e2105080118, doi:10.1073/pnas.2105080118.

Leeson A A, Forster E, Rice A, et al. 2020. Evolution of supraglacial lakes on the Larsen B Ice Shelf in the decades before it collapsed. Geophys Res Lett, 47(4): e2019GL085591, doi:10.1029/2019gl085591.

Leprince S, Ayoub F, Klinger Y, et al. 2008. Co-Registration of Optically Sensed Images and Correlation (COSI-Corr): an operational methodology for ground deformation measurements. 2007 IEEE International Geoscience and Remote Sensing Symposium. July 23-28, 2007, Barcelona, Spain. IEEE, 1943-1946, doi:10.1109/IGARSS.2007.4423207.

Levermann A, Albrecht T, Winkelmann R, et al. 2012. Kinematic first-order calving law implies potential for abrupt ice-shelf retreat. Cryosphere, 6(2): 273-286, doi:10.5194/tc-6-273-2012.

Li D A, Jiang L M, Huang R G. 2021. Hydrological and kinematic precursors of the 2017 calving event at the petermann glacier in Greenland observed from multi-source remote sensing data. Remote Sens, 13(4): 591, doi:10.3390/rs13040591.

Lipovsky B P. 2020. Ice shelf rift propagation: stability, three-dimensional effects, and the role of marginal weakening. Cryosphere, 14(5): 1673-1683, doi:10.5194/tc-14-1673-2020.

Lüttig C, Neckel N, Humbert A. 2017. A combined approach for filtering ice surface velocity fields derived from remote sensing methods. Remote Sens, 9(10): 1062, doi:10.3390/rs9101062.

MacAyeal D R. 1989. Large-scale ice flow over a viscous basal sediment: theory and application to ice stream B, Antarctica. J Geophys Res, 94(B4): 4071-4087, doi:10.1029/jb094ib04p04071.

MacGregor J A, Catania G A, Markowski M S, et al. 2012. Widespread rifting and retreat of ice-shelf margins in the eastern Amundsen Sea Embayment between 1972 and 2011. J Glaciol, 58(209): 458-466, doi:10.3189/2012jog11j262.

Markus T, Neumann T, Martino A, et al. 2017. The Ice, Cloud, and land Elevation Satellite-2 (ICESat-2): science requirements, concept, and implementation. Remote Sens Environ, 190: 260-273, doi:10.1016/j.rse.2016.12.029.

Marsh O J, Price D, Courville Z R, et al. 2021. Crevasse and rift detection in Antarctica from TerraSAR-X satellite imagery. Cold Reg Sci Technol, 187: 103284, doi:10.1016/j.coldregions.2021.103284.

Millan R, Mouginot J, Derkacheva A, et al. 2022. Ongoing grounding line retreat and fracturing initiated at the Petermann Glacier ice shelf, Greenland, after 2016. Cryosphere, 16(7): 3021-3031, doi:10.5194/tc-16-3021-2022.

Morlighem M, Bondzio J, Seroussi H, et al. 2016. Modeling of Store Gletscher's calving dynamics, West Greenland, in response to ocean thermal forcing. Geophys Res Lett, 43(6): 2659-2666, doi:10.1002/2016gl067695.

Morlighem M, Williams C N, Rignot E, et al. 2017. BedMachine v3: complete bed topography and ocean bathymetry mapping of Greenland from multibeam echo sounding combined with mass conservation. Geophys Res Lett, 44(21): 11051-11061, doi:10.1002/2017gl074954.

Mouginot J, Scheuchl B, Rignot E. 2012. Mapping of ice motion in Antarctica using synthetic-aperture radar data. Remote Sens, 4(9): 2753-2767, doi:10.3390/rs4092753.

Münchow A, Padman L, Fricker H A. 2014. Interannual changes of the floating ice shelf of Petermann Gletscher, North Greenland, from 2000 to 2012. J Glaciol, 60(221): 489-499, doi:10.3189/2014jog13j135.

Nick F M, Luckman A, Vieli A, et al. 2012. The response of Petermann Glacier, Greenland, to large calving events, and its future stability in the context of atmospheric and oceanic warming. J Glaciol, 58(208): 229-239, doi:10.3189/2012jog11j242.

Pattyn F, Morlighem M. 2020. The uncertain future of the Antarctic Ice Sheet. Science, 367(6484): 1331-1335, doi:10.1126/science.aaz5487.

Porter C, Howat I, Noh M J, et al. 2022. ArcticDEM – Strips, Version 4.1. (2022-10-11) [2023-02-10]. doi:10.7910/DVN/C98DVS.

Pörtner H O, Debra C R, Valérie M D, et al. 2019. IPCC special report on the ocean and cryosphere in a changing climate. Cambridge: Cambridge University Press.

Rignot E, Kanagaratnam P. 2006. Changes in the velocity structure of the Greenland ice sheet. Science, 311(5763): 986-990, doi:10.1126/science.1121381.

Rignot E, Steffen K. 2008. Channelized bottom melting and stability of floating ice shelves. Geophys Res Lett, 35(2): L02503, doi:10.1029/2007gl031765.

Robel A A, Banwell A F. 2019. A speed limit on ice shelf collapse through hydrofracture. Geophys Res Lett, 46(21): 12092-12100, doi:10.1029/2019gl084397.

Rückamp M, Neckel N, Berger S, et al. 2019. Calving induced speedup of petermann glacier. JGR Earth Surface, 124(1): 216-228, doi:10.1029/2018jf004775.

Stocker T, Qin D H, Plattner G, et al. 2013. Climate change 2013: the physical science basis. New York: Cambridge University Press.

Straneo F, Heimbach P. 2013. North Atlantic warming and the retreat of Greenland's outlet glaciers. Nature, 504(7478): 36-43, doi:10.1038/nature12854.

Vieli A, Funk M, Blatter H. 2001. Flow dynamics of tidewater glaciers: a numerical modelling approach. J Glaciol, 47(159): 595-606, doi:10.3189/172756501781831747.

Vieli A, Payne A J, Shepherd A, et al. 2007. Causes of pre-collapse changes of the Larsen B Ice Shelf: numerical modelling and assimilation of satellite observations. Earth Planet Sci Lett, 259(3-4): 297-306, doi:10.1016/j.epsl.2007.04.050.

Washam P, Nicholls K W, Münchow A, et al. 2019. Summer surface melt thins Petermann Gletscher Ice Shelf by enhancing channelized basal melt. J Glaciol, 65(252): 662-674, doi:10.1017/jog.2019.43.

Zarrinderakht M, Schoof C, Peirce A. 2022. The effect of hydrology and crevasse wall contact on calving. Cryosphere, 16(10): 4491-4512, doi:10.5194/tc-16-4491-2022.

# Supplementary Figure

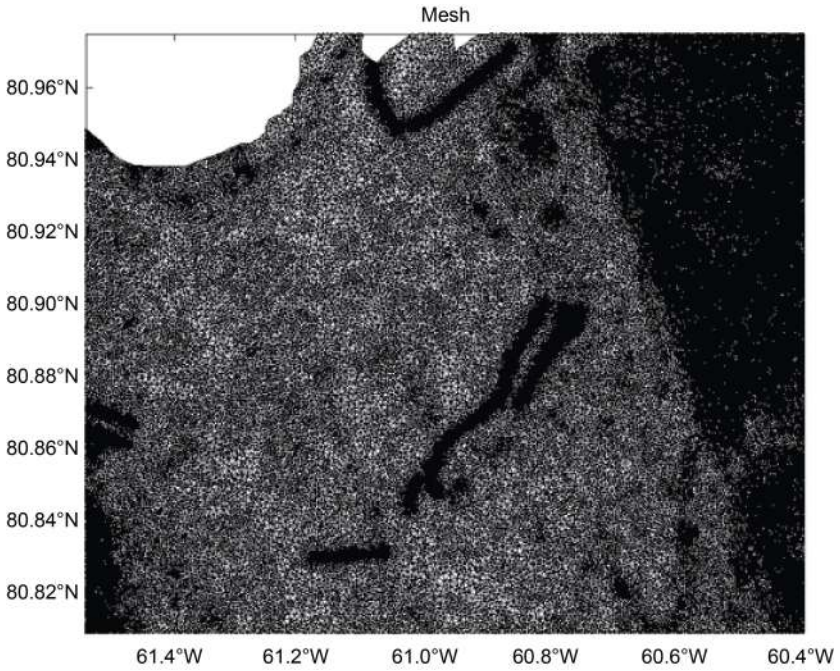


**Figure S1** The model mesh. The finite element grids presented the fast-flowing, slow-moving, and the fracture of floating ice, which were performed on an adaptive finite element grid, with a high resolution of 50 m in fast-flowing regions and a coarser resolution of 2000 m in the slow-moving region. For the fracture of floating ice, the region was refined with a mesh resolution of 20 m. In total, the mesh was made up of about 110676 elements.